Gas-liquid mass transfer around a Taylor bubble during the formation and flowing stage in a square flow-focusing milli-channel

Mei Mei, Gilles Hebrard, Karine Loubière, Nicolas Dietrich

Proceedings of the 15th International Conference on Gas-Liquid
and Gas-Liquid-Solid Reactor Engineering (GLS-15)
August 8-11, 2021
Ottawa, Canada

Gas-liquid mass transfer around a Taylor bubble during the formation and flowing stage in a square flow-focusing milli-channel

Mei Mei[1,2,3], Gilles Hébrard[1,3], Karine Loubière[2,3*], Nicolas Dietrich[1,3],
[1] *Toulouse Biotechnology Institute, Université de Toulouse, CNRS, INRAE, INSA, Toulouse, France*
[2] *Laboratoire de Génie Chimique, Université de Toulouse, CNRS, INP, UPS, Toulouse, France*
[3] *Fédération de Recherche FERMAT, CNRS, Toulouse, France*
*Corresponding author(s): nicolas.dietrich@insa-toulouse.fr

Summary

This present work aims at studying the gas-liquid mass transfer around a Taylor bubble during the bubble formation stage and just after. For this purpose, the resazurin-based colorimetric technique proposed by Dietrich et al. (2013) was applied in a square flow-focusing milli-channel. An original MATLAB program was developed to extract first the features of two-phase flow pattern, such as: the bubble length and velocity, the liquid slug length, and secondly the equivalent oxygen concentration fields inside the liquid phase by means of an ad hoc calibration procedure.. This study showed that, the equivalent O_2 concentration fields in the liquid slugs right after the bubble formation presents complex patterns (three-dimensional and transitory). At a given liquid flow rate, an increase of gas-liquid flow rate ratio led to higher levels of accumulated equivalent O_2 concentration fields in the liquid slugs. At a given gas-liquid flow rate ratio, decreasing liquid flow rates allowed to a rise of the accumulated equivalent O_2 concentration fields in the liquid slugs. At last, the contribution of the bubble formation to the overall mass transfer was found significant.

Keywords: Gas-liquid mass transfer, Taylor bubble formation, resazurin-based colorimetric method, flow-focusing milli-channel.

Introduction

Continuous-flow micro-structured technologies have emerged as alternatives to batch processing. Their implementation in process intensification has proven particularly beneficial in terms of sustainable chemistry and processes. They present several significant advantages over conventional reactors, such as smaller volumes, higher surface to volume ratios and enhanced mass and heat transfer (Haase et al., 2016). Gas-liquid reactive flows are widely encountered in chemical industry, (i.e. hydrogenations, sensitized photo-oxygenations or photo-redox catalysis reactions, fluorinations and biochemical reactions).

The microtechnology devices allow producing highly regular, repeatable and mono-dispersed bubbles and liquid slugs. Such flow patterns, commonly named Taylor flows, presents very interesting features for carrying out, under controlled conditions, multiphase reactions involving out competitive and/or consecutive reactional schemes. The bubble formation process (initial step) has been investigated through lots of experimental and simulation methods (Fu and Ma, 2015), because the question of "when and how bubble pinch-off happens" directly determines the bubble size and frequency (Dang et al., 2013). The main factors influencing the bubble pinch-off were found as following: the confinement space (i.e., channel geometry) (Dietrich et al., 2008; Garstecki et al., 2006), the gas-liquid flow rate ratio (Garstecki et al., 2006), the viscosity of the liquid phase (Lu et al., 2014b; Zhang et al., 2017), interfacial tension (Lu et al., 2014a) between two phases, rheological property (Fu et al., 2011a, b; Fu et al., 2012) of the liquid phase and surfactants (Li et al., 2020), etc. The channel geometry gather various parameters, including the inlet geometry (e.g. T-junction, flow-focusing and co-flowing geometries), wettability of channel and cross-sectional shapes (Garstecki et al., 2006).

The bubble formation mechanisms in microfluidic devices were commonly classified into three patterns (Fu and Ma, 2015), i.e., squeezing, dripping (shearing), and jetting regimes (Xu et al., 2008). The different bubble breakup patterns were influenced by the balance between the exerted forces acting on gas thread, i.e., surface tension force, viscous shear force and inertia force (Dollet et al., 2008), etc. Among these regimes, the jetting regime of bubble formation (Castro-Hernández et al., 2011; De Menech et al., 2008; Fu et al., 2009) was less reported than others in confined microdevices (T-junction or flow-focusing with cross sections) but more reported in unconfined microdevices (Xu et al., 2014). In squeezing regime (Garstecki et al., 2006), the gas phase penetrates into the main channel, propagates towards the wall and downstream, resulting in a blockage of continuous flow. Due to this blockage, the induced increased pressure force at the upstream of the slug finally triggers the breakup. The interfacial force dominates the viscous force, i.e., low capillary numbers. In shearing (dripping) regimes, bubbles pinching occurrs under the dominant viscous shear force compared to the surface tension force, i.e., high capillary numbers. The transition between these two regimes occurs for a critical number almost equal to 10^{-2} (De Menech et al., 2008; Garstecki et al., 2006), above which the viscous shear force starts to make a major role in bubble formation process. Later (Xu et al., 2008) and Fu et al. (2010) further specified the Ca number ranges for these two regimes. They observed that the Ca number ranges for squeezing and dripping regime were at (10^{-4}, 0.0058) and (0.013, 0.1), respectively. In addition, Xu et al. (2008) and Fu et al. (2010) investigated the 'squeezing

to dripping' transition, in which both squeezing pressure and the shear force affect the collapse, and this transition regimes occurred at a medium range of Ca ∈(0.0058, 0.013).

However, few works are devoted to investigate the role of the bubble formation step into the overall gas-liquid mass transfer process. Fries and Rohr (2009) specifically investigated the effects of inlet geometry on mass transfer, and showed that a carefully designed inlet geometry could enhance mass transfer by varying unit cell lengths. Tan et al. (2012) and Yang et al. (2016b) then quantified a large contribution (45-90%) when compared to the overall bubble flowing stage. Mei et al. (2020b) observed that a progressive decrease of the transferred flux along the channel's length until reaching a plateau, confirming the occurrence of strong inlet effects related to the bubble formation step. From these works, one can conclude that, up to now, neither the detailed mechanisms controlling the amount of species transferred from the bubble to the liquid phase during and right after the bubble formation step nor the related contribution are well clearly evaluated.

Therefore, this study proposes to fill this gap by implementing the resazurin-based colorimetric method in a dedicated experimental set-up allowing to visualize and quantify he gas-liquid mass transfer during and right after the bubble formation step

Experimental and Numerical Methods

Experimental set-up

The experimental set-up is illustrated in Figure 1 (a) and (b). The device was fabricated in a transparent polymethylmethacrylate (PMMA) plate (100×600×2mm) and sandwiched by other two PMMA plates (100×600×4mm) with screws and sealing rings. The inlet geometry of the microchannel is a flow-focusing channel. All the channels, including the injection inlets of gas and liquid, and the main channel, have the same square cross section (w^2=2×2 mm$^{2)}$. The length of the gas inlet, liquid inlet, and main channels are 70 mm, 50 mm, and 530 mm, respectively. The camera was fixed at two observing positions, as shown in Figure 1 (c), to investigate the mass transfer during the bubble formation state and steady bubble flowing stage, respectively.

Air, as gas phase, is fed from house compressed air lines and its flow rates are controlled by a DPC17S-V0L6-BB5 airflow controller. Liquid solutions are both supplied from a 60 mL syringe in a syringe pump (Harvard Apparatus, PHD 22/2000, USA). The gas was introduced from the main channel and the liquid were injected from two side channels at the same flow rates. After changing to a new flow rate, at least two times of residence time of milli-channel were assured to reach a steady state, which was verified by the camera through the bubble and liquid slug length. A Unisense oxygen microsensor multimeter is connected at the outlet of the channel to monitor the oxygen concentration.

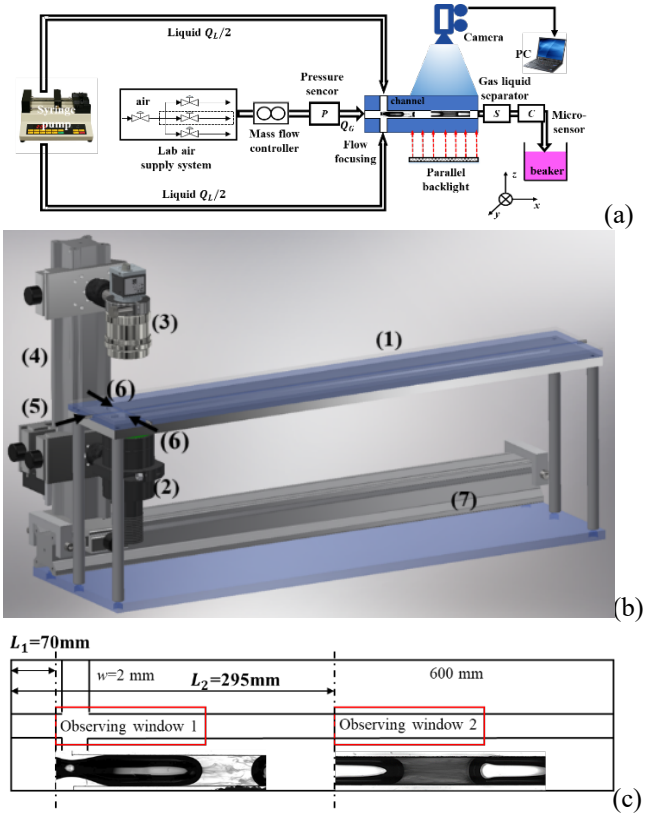

Figure 1: (a) Schematic representations of the experimental set-up; (b) experimental setup 3D schema (1) the milli-channel (2) the backlight panel (3) high-speed camera (4) support of Camera and backlight (5) gas inlet (6) liquid inlet (7) sliding support; (c) positions of two observing windows.

Resazurin is chosen as the oxygen-sensitive dye, which can be irreversibly reduced to resorufin and furtherly to dihydroresorufin in alkaline solution containing glucose. The dihydroresorufin, presenting colorless, could be reversibly oxidized into the resorufin by oxygen, which presents an intense pink color. The aqueous phase was composed of D-glucose anhydrous (Sigma Aldrich, CAS 50-99-7) at a concentration of 20 $g\,L^{-1}$, sodium hydroxide (Sigma Aldrich, CAS 1310-73-2) at a concentration of 20 $g\,L^{-1}$, and resazurin (Sigma Aldrich, CAS 199303, purity 93%, noted as RZ) at a concentration of 0.093 $g\,L^{-1}$ (corresponding to 0.1 $g\,L^{-1}$ of weighted resazurin).

Images of gas-liquid flow lighted by a M530L4 LED were recorded by a Basler acA2040-90 camera. The LED excitation wavelength is at 530nm. After the LED, a specific lens was designed to generate parallel light. The camera was set to work at a recording rate of 200 frames/s with an exposure time of 28 μs and a resolution of 1280×512 pixels. The spatial resolution of the images was at 1.5 μm per pixel. All experiments were conducted under atmospheric pressure at a temperature controlled (20° C) room, and for several conditions of Reynolds, Capillary and Weber numbers, enabling to cover a large range of bubble size.

Gas-liquid hydrodynamics image processing

After detecting the bubble and liquid slug images, an original MATLAB program was developed to extract the hydrodynamic characteristics for Taylor flows, referring to

Mei et al. (2020a). Bubble lengths and liquid slug lengths, averaged within the observing window, were measured using 100 image frames, and noted as $\langle L_B \rangle$ and $\langle L_S \rangle$ (see Figure 2). The instantaneous bubble velocity was calculated from the distance travelled by the bubble centroid between two consecutive images, divided by the acquisition time. The mean bubble velocity, $\langle U_B \rangle$, was then calculated by averaging the obtained bubble velocities by considering 100 consecutive image frames.

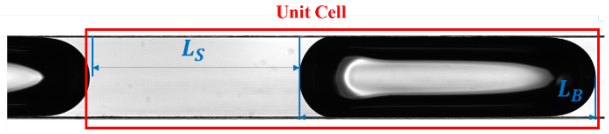

Figure 2: Representation of bubble and liquid slug lengths.

Gas-liquid mass transfer image processing

The resazurin-based colorimetric method was implemented according to the procedure described by Dietrich et al. (2013). After the image acquisition, the gas-liquid mass transfer characteristics were determined through three main image processing steps (implemented in MATLAB R2017b®): (i) extraction of liquid slugs and bubbles from the images; (ii) determination of the calibration curve; and (iii) conversion, pixel-by-pixel, of the gray values in the liquid slugs into equivalent oxygen concentrations. The first step is referred to Mei et al. (2020b). The term "equivalent" is used, because in reality, the oxygen concentration in the liquid phase was zero: oxygen was fully consumed by dihydroresorufin (see(Yang et al., 2016a).

For the calibration process, five sets of RZ solutions at different concentrations were prepared: 0.01, 0.02, 0.05, 0.08 and 0.10 g L^{-1} (93% purity). At each concentration, 200 frames of the channel in which the solution (i.e., pink RF) fully saturated flowed, were taken. This process was repeated three times with solutions of the same concentration to reduce experimental uncertainties. Finally, for each RZ concentration, a time-averaged gray value image was obtained by averaging the 200 images to eliminate the slight deviation between instantaneous gray values. Typical averaged gray image of different RZ concentrations are shown in Figure 3 (a). To overcome the non-uniform distribution issue, a pixel-by-pixel calibration was applied to minimize the errors, which meant that the calibration relation curve was calculated independently, pixel by pixel.

In this study, the equivalent concentration of the O_2 is converted based on the Beer-Lambert law, as shown in Equation (1).

$$A = -ln\frac{I}{I_0} = \varepsilon l C \qquad (1)$$

where A and l are the absorbance and the optical path length, ε and C represent the molar attenuation coefficient and the concentration of the attenuating species (i.e., RF). I and I_0 represent the intensities of the measured RF solution and the reference base solution without RF (glucose in alkaline solution). Therefore, according to the Beer-Lambert law, the concentrations of RF are proportional to the variations of absorbance.

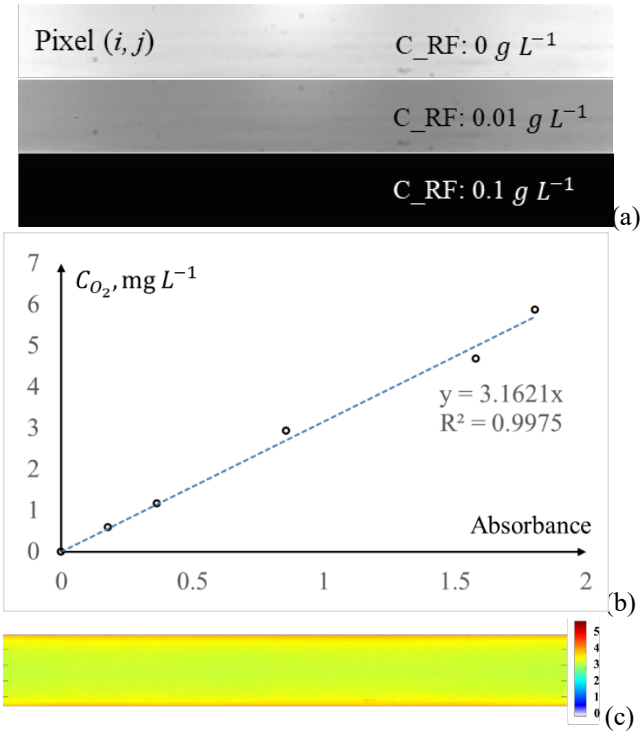

Figure 3: (a) Typical averaged gray images of different RZ concentrations; (b) a representation of one calibration curve between absorbance and equivalent oxygen concentrations; (c) the calibration coefficients K_{ij} fields at observing window 2.

In addition, combined with the stoichiometry of the reaction between DH and O_2, the relations between RF concentration and the variations of absorbance could be converted to the oxygen concentrations versus the variations of absorbance. Figure 3 (b) shows a typical relation for a given pixel between the equivalent O_2 concentration and the absorbance value, A. And the relation for one pixel is shown in equation (2).

$$C_{O_2}(i,j) = K_{i,j}A = K_{i,j}ln\frac{I_0}{I} \qquad (2)$$

where $C_{O_2}(i,j)$ is the equivalent O_2 concentration; $K_{i,j}$ is the calibration coefficient for one pixel (i, j). And the calculated $K_{i,j}$ for all pixels at observing window 2 are shown in Figure 3 (c). It can be seen that the $K_{i,j}$ coefficients are almost uniform near the channel center, and present higher values near the channel wall due to the refraction and reflection of the wall.

Results and Discussion

Gas-liquid hydrodynamics

Figure 4 (a) and (b) show the variation of the average dimensionless bubble length, $\langle L_B \rangle / w$, and liquid slug length, $\langle L_S \rangle / w$, as a function of the gas-liquid flow rate ratio (noted as η) and the inverse of η for two observing windows, respectively. The angle brackets symbol "⟨ ⟩" is used to represent the average value in the observing windows of bubble formation and flowing stage.

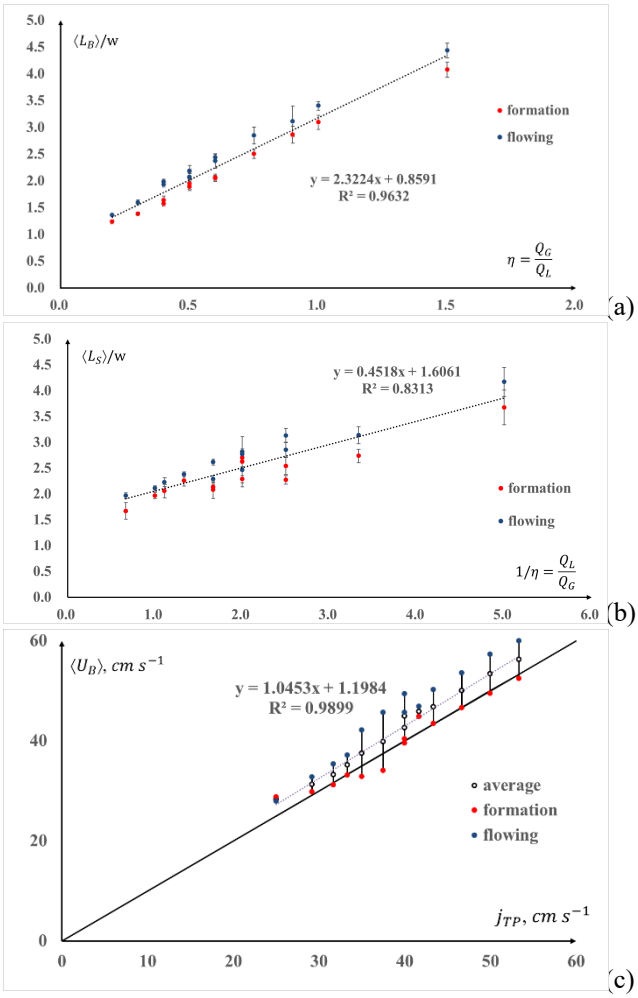

Figure 4: (a) Average dimensionless bubble length $\langle L_B \rangle/w$ versus gas-liquid flow rate ratio η and (b) average dimensionless liquid slug length $\langle L_S \rangle/w$ versus the inverse of η; (c) average bubble velocities $\langle U_B \rangle$ under various total superficial velocities j_{TP}.

As expected, the average bubble and slug lengths increased linearly with η and the inverse of η respectively, The observed $\langle L_B \rangle/w$ and $\langle L_S \rangle/w$ dimensionless lengths at bubble formation stage were smaller than those at bubble flowing stage, which may be caused by the non-fully steady development of the Taylor flow during the bubble formation. It can be seen that the linear scaling laws of bubble and liquid slug length indicate the bubble formation under $\eta \in (0.2, 1.5)$ was dominated by squeezing mechanism (Garstecki et al., 2006; Lu et al., 2014b).

Figure 4 (c) reports the averaged bubble velocity, $\langle U_B \rangle$, versus the total superficial velocity, j_{TP} (calculated at the inlet conditions), for two stages of bubble formation and bubble flowing. Generally, the averaged bubble velocities were almost 1.05 times of the j_{TP}, which indicates that there was thin liquid lubrication film around the Taylor bubbles. This is in accordance with the previous study in square channels (Kreutzer et al., 2005). Furthermore, the mean bubble velocities in the steady bubble flowing stage were higher than $\langle U_B \rangle$ in bubble formation stage, which suggest more liquid film were developed after the bubble formation stage.

All the results of $\langle L_B \rangle/w$, $\langle L_S \rangle/w$ and $\langle U_B \rangle$ follow the identical trends for two stages of bubble formation and flowing, which validates the uniformity and regularity of the generated Taylor bubbles and liquid slugs.

Gas-liquid mass transfer

By implementing the RZ-based colorimetric method, the variations of intensities inside the liquid slug could be converted to equivalent O_2 concentration values using the law calibration.

Figure 5 (a) and (b) show typical raw images of the mass transfer process during the bubble formation and flowing stages, respectively. During the bubble formation stage, the oxygen was accumulated at the bubble nose near centerline and bubble rear near the wall. At the steady bubble flowing stage, the grey values inside the liquid slug was almost uniform, which suggests an efficient mixing due to recirculation loops in liquid slug.

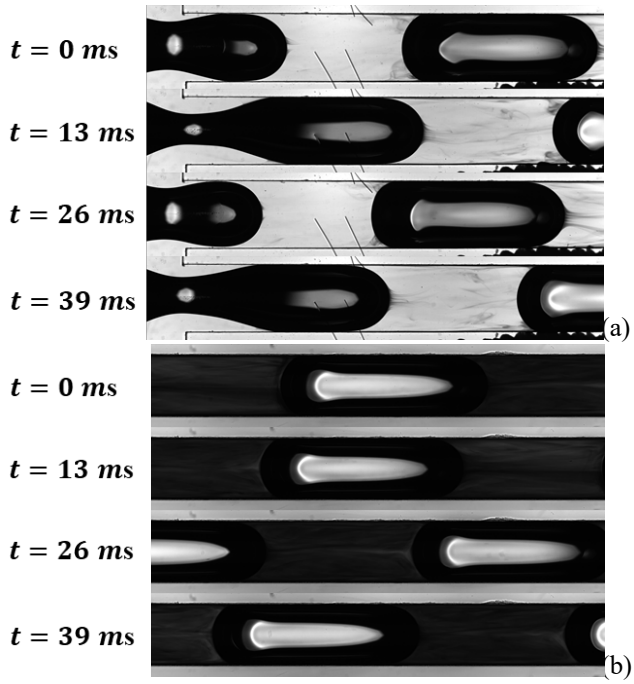

Figure 5: Typical images of the mass transfer process (Q_L=Q_G=40 mL min^{-1}). (a) bubble formation stage (b) bubble flowing stage.

Figure 6 presents the equivalent O_2 concentration fields in the liquid slugs right after the bubble formation. The liquid close to the centerline of the channel move forwards (i.e., right) while the liquid close to the wall move backwards (i.e., left), resulting in toroidal motion inside the slug. Due to symmetry of the cross-flow focusing channel, the vortex was kept symmetry along the channel. From Figure 6 (a), (b) to (c), increasing Q_L and Q_G, (i.e., Re_{TP}), made more complex the vortex developed with non-symmetry along channel.

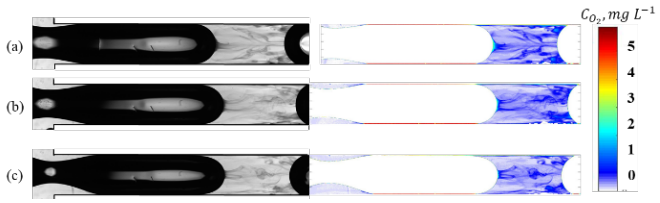

Figure 6: Raw images of RF signal and the corresponding converted instantaneous equivalent O_2 concentration fields inside of the liquid slug right after the bubble formation for several operating conditions: (a) $Q_L = 20\ mL\ min^{-1}$, $Q_G = 48\ mL\ min^{-1}$, Re_{TP}=509; (b) $Q_L = 30\ mL\ min^{-1}$, $Q_G = 60\ mL\ min^{-1}$, Re_{TP}=674; (c) $Q_L = 40\ mL\ min^{-1}$, $Q_G = 70\ mL\ min^{-1}$, Re_{TP}=824.

Figure 7 presents the equivalent O_2 concentration fields in the liquid slugs of the bubble formation stage at the left column and of the bubble flowing stage at the right column. At the given gas-liquid flow rate ratio η equal to 0.5, with the increase of the liquid flow rate Q_L, the equivalent O_2 concentrations became smaller due to lower residence time at the same position, no matter at the bubble stage or bubble flowing stage. Meanwhile, the equivalent O_2 concentration fields in liquid slugs became more uniform with the increase of the liquid flow rate Q_L at the given η equals to 0.5.

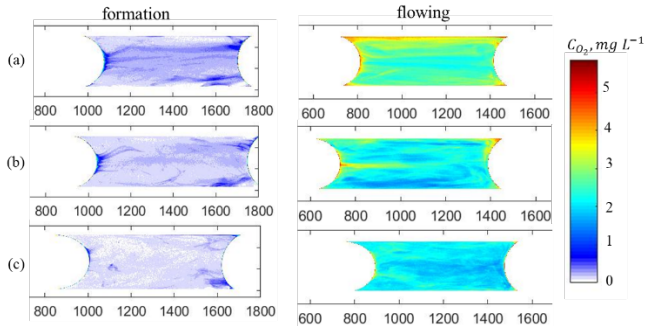

Figure 7: Equivalent O_2 concentration field inside of the liquid slug right after the bubble formation for several operating conditions for at η=0.5, (a) $Q_L = 40\ mL\ min^{-1}$; (b) $Q_L = 60\ mL\ min^{-1}$; (c) $Q_L = 80\ mL\ min^{-1}$.

To give a quantified comparison of the equivalent O_2 concentration in liquid slug for bubble formation and bubble flowing stages, Figure 8 (a) and (b) summarize their values respectively under various operating conditions. Generally, at a given the liquid flow rate Q_L, with the increase of gas-liquid flow rate ratio η, the accumulated equivalent O_2 concentration fields in the liquid slugs were increasing for bubble formation and bubble flowing stages, except for η=0.5 and 0.6 for Q_L=80 mL min^{-1}. This could be explained by the compensate effects of increased mass transfer and shortened residence time. At a given gas-liquid flow rate ratio η, with the increase of the liquid flow rate Q_L, the accumulated equivalent O_2 concentration fields in the liquid slugs were decreasing for bubble formation and bubble flowing stages. The cumulated equivalent O_2 concentration here represents the effective transferred O_2 into the liquid slug, further mass transfer coefficients should be related to the specific gas-liquid interfacial area.

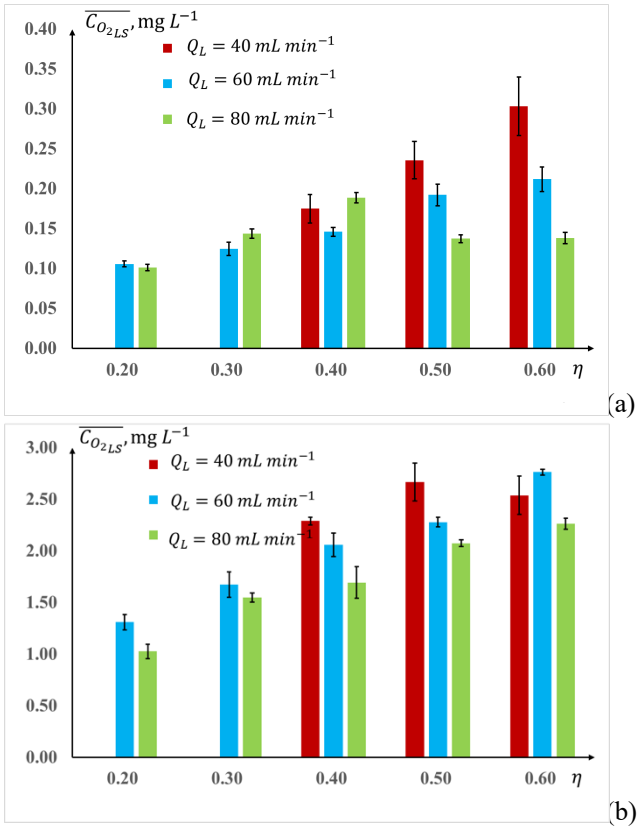

Figure 8 (a) Equivalent O_2 concentration in liquid slug versus η for bubble formation stage; (b) equivalent O_2 concentration in liquid slug versus η for bubble flowing stage, under various Q_L equal to 40, 60 and 80 mL min^{-1}.

Conclusions

The aim of this original experimental study was to investigate gas-liquid mass transfer around Taylor bubbles (air) during bubble formation and flowing stages in cross-flowing milli-channel. Using the resazurin-based colorimetric technique and image processing, the equivalent oxygen concentration fields are visualized and measured during the bubble formation process (observing window 1), and after the detachment when bubbles flow in the milli-channel (observing window 2). The main findings are as following:

(1) The average dimensionless bubble length, $\langle L_B \rangle/w$, and liquid slug length, $\langle L_S \rangle/w$, follow the linear scaling laws with the gas-liquid flow rate ratio η and the inverse of η, respectively;

(2) The equivalent O_2 concentration fields in the liquid slugs right after the bubble formation presents complicated patterns instead of Taylor recirculation loops due to high Re_{TP} numbers. Generally, at the given Q_L, with the increase of η, the equivalent O_2 concentration fields in the liquid slugs were increasing for bubble formation and bubble flowing stages. At the given η, with the increase of Q_L, the accumulated equivalent O_2 concentration fields in the liquid slugs were decreasing for bubble formation and bubble flowing stages.

Further studies of the gas-liquid mass transfer coefficients will be implemented in the future.

Acknowledgments

The authors would like to acknowledge the financial assistance provided by the China Scholarship Council.

References

Castro-Hernández, E., Van Hoeve, W., Lohse, D., Gordillo, J.M., 2011. Microbubble generation in a co-flow device operated in a new regime. Lab on a Chip - Miniaturisation for Chemistry and Biology 11, 2023-2029.

Dang, M., Yue, J., Chen, G., Yuan, Q., 2013. Formation characteristics of Taylor bubbles in a microchannel with a converging shape mixing junction. Chemical Engineering Journal 223, 99-109.

De Menech, M., Garstecki, P., Jousse, F., Stone, H.A., 2008. Transition from squeezing to dripping in a microfluidic T-shaped junction. Journal of Fluid Mechanics 595, 141-161.

Dietrich, N., Loubière, K., Jimenez, M., Hébrard, G., Gourdon, C., 2013. A new direct technique for visualizing and measuring gas–liquid mass transfer around bubbles moving in a straight millimetric square channel. Chemical Engineering Science 100, 172-182.

Dietrich, N., Poncin, S., Midoux, N., Li, H.Z., 2008. Bubble formation dynamics in various flow-focusing microdevices. Langmuir 24, 13904-13911.

Dollet, B., Van Hoeve, W., Raven, J.-P., Marmottant, P., Versluis, M., 2008. Role of the channel geometry on the bubble pinch-off in flow-focusing devices. Physical Review Letters 100, 034504.

Fries, D.M., Rohr, P.R.V., 2009. Impact of inlet design on mass transfer in gas–liquid rectangular microchannels. Microfluidics and Nanofluidics 6, 27-35.

Fu, T., Ma, Y., 2015. Bubble formation and breakup dynamics in microfluidic devices: A review. Chemical Engineering Science 135, 343-372.

Fu, T., Ma, Y., Funfschilling, D., Li, H.Z., 2009. Bubble formation and breakup mechanism in a microfluidic flow-focusing device. Chemical Engineering Science 64, 2392-2400.

Fu, T., Ma, Y., Funfschilling, D., Li, H.Z., 2011a. Bubble formation in non-Newtonian fluids in a microfluidic T-junction. Chemical Engineering and Processing 50, 438-442.

Fu, T., Ma, Y., Funfschilling, D., Li, H.Z., 2011b. Gas-liquid flow stability and bubble formation in non-Newtonian fluids in microfluidic flow-focusing devices. Microfluidics and Nanofluidics 10, 1135-1140.

Fu, T., Ma, Y., Funfschilling, D., Zhu, C., Li, H.Z., 2010. Squeezing-to-dripping transition for bubble formation in a microfluidic T-junction. Chemical Engineering Science 65, 3739-3748.

Fu, T., Ma, Y., Funfschilling, D., Zhu, C., Li, H.Z., 2012. Breakup dynamics of slender bubbles in non-newtonian fluids in microfluidic flow-focusing devices. AIChE Journal 58, 3560-3567.

Garstecki, P., Fuerstman, M.J., Stone, H.A., Whitesides, G.M., 2006. Formation of droplets and bubbles in a microfluidic T-junction - scaling and mechanism of break-up. Lab on a Chip 6, 437-446.

Haase, S., Murzin, D.Y., Salmi, T., 2016. Review on hydrodynamics and mass transfer in minichannel wall reactors with gas–liquid Taylor flow. Chemical Engineering Research and Design 113, 304-329.

Kreutzer, M.T., Kapteijn, F., Moulijn, J.A., Heiszwolf, J.J., 2005. Multiphase monolith reactors: chemical reaction engineering of segmented flow in microchannels. Chemical Engineering Science 60, 5895-5916.

Li, X., Huang, Y., Chen, X., Sunden, B., Wu, Z., 2020. Breakup dynamics of gas-liquid interface during Taylor bubble formation in a microchannel flow-focusing device. Experimental Thermal and Fluid Science 113, 110043.

Lu, Y., Fu, T., Zhu, C., Ma, Y., Li, H.Z., 2014a. Pinch-off mechanism for Taylor bubble formation in a microfluidic flow-focusing device. Microfluidics and Nanofluidics 16, 1047-1055.

Lu, Y., Fu, T., Zhu, C., Ma, Y., Li, H.Z., 2014b. Scaling of the bubble formation in a flow-focusing device: Role of the liquid viscosity. Chemical Engineering Science 105, 213-219.

Mei, M., Felis, F., Dietrich, N., Hébrard, G., Loubière, L., 2020a. Hydrodynamics of gas-liquid slug flows in a long in-plane spiral-shaped milli-reactor. Theoretical Foundations of Chemical Engineering 54, 25-47.

Mei, M., Hébrard, G., Dietrich, N., Loubière, K., 2020b. Gas-liquid mass transfer around Taylor bubbles flowing in a long, in-plane, spiral-shaped milli-reactor. Chemical Engineering Science 222, 115717.

Tan, J., Lu, Y.C., Xu, J.H., Luo, G.S., 2012. Mass transfer characteristic in the formation stage of gas-liquid segmented flow in microchannel. Chemical Engineering Journal 185, 314-320.

Xu, J.H., Li, S., Tan, J., Luo, G., 2008. Correlations of droplet formation in T-junction microfluidic devices: from squeezing to dripping. Microfluidics and Nanofluidics 5, 711-717.

Xu, K., Tostado, C.P., Xu, J.H., Lu, Y.C., Luo, G.S., 2014. Direct measurement of the differential pressure during drop formation in a co-flow microfluidic device. Lab on a Chip 14, 1357.

Yang, L., Dietrich, N., Loubière, K., Gourdon, C., Hébrard, G., 2016a. Optical methods to investigate the enhancement factor of an oxygen-sensitive colorimetric reaction using microreactors. AIChE Journal.

Yang, L., Dietrich, N., Loubière, K., Gourdon, C., Hébrard, G., 2016b. Visualization and characterization of gas-liquid mass transfer around a Taylor bubble right after the formation stage in microreactors. Chemical Engineering Science 143, 364-368.

Zhang, C., Fu, T., Zhu, C., Jiang, S., Ma, Y., Li, H.Z., 2017. Dynamics of bubble formation in highly viscous liquids in a flow-focusing device. Chemical Engineering Science 172, 278-285.